Research
Environmental Engineering—Article

PbS Quantum Dot Image Sensors Derived from Spent Lead-Acid Batteries via an Environmentally Friendly Route

Yuxin Tong [a,b,#], Dijie Zhang [c], Zhaoyang Li [a,b,#], Guang Hu [a,b], Qingfang Zou [a,b], Luna Xiao [c], Weidong Wu [c], Liang Huang [a,b], Sha Liang [a,b], Huabo Duan [a,b], Jingping Hu [a,b], Huijie Hou [a,b], Jianbing Zhang [c,*], Jiakuan Yang [a,b,d,*]

[a] Hubei Key Laboratory of Multi-media Pollution Cooperative Control in Yangtze Basin, School of Environmental Science and Engineering, Huazhong University of Science and Technology (HUST), Wuhan 430074, China
[b] Hubei Provincial Engineering Laboratory of Solid Waste Treatment, Disposal and Recycling, Wuhan 430074, China
[c] School of Integrated Circuits, Wuhan National Laboratory for Optoelectronics, Huazhong University of Science and Technology (HUST), Wuhan 430074, China
[d] State Key Laboratory of Coal Combustion, Huazhong University of Science and Technology (HUST), Wuhan 430074, China

ABSTRACT

PbS quantum dot (QD) image sensors have emerged as promising chips for a wide range of infrared (IR) imaging applications due to their monolithic integration with silicon-based readout integrated circuits. However, avoiding primary toxic Pb usage and reducing the cost of PbS QDs remains crucial for widespread application. We present a novel cost-effective and environmentally friendly hydrometallurgical process for recovering $PbCl_2$ from spent lead-acid battery paste to synthesize high-quality PbS QDs. The method recovers $PbCl_2$ with a production ratio of 97% and a purity of 99.99%. PbS QDs and photodetectors synthesized from recycled $PbCl_2$ (R-$PbCl_2$) have comparable performance and quality to those made using commercial $PbCl_2$. R-$PbCl_2$-derived photodetectors exhibit a high external quantum efficiency of 49.6% and a high specific detectivity of 6.95×10^{12} Jones compared to published studies. Additionally, based on R-$PbCl_2$, a PbS QD image sensor with 640×512 resolution successfully discriminated common solvents. Moreover, through life-cycle assessment and economic cost analysis, this novel synthesis route offers great advantages in the environmentally friendly use of chemical reagents and reduces the production cost of PbS QDs by 23.2% compared to commercial $PbCl_2$. Thus, this work not only contributes to the green recycling of spent lead paste but also provides a low-cost strategy for synthesizing PbS QDs and their optoelectronic application.

© 2024 THE AUTHORS. Published by Elsevier LTD on behalf of Chinese Academy of Engineering and Higher Education Press Limited Company. This is an open access article under the CC BY-NC-ND license (http://creativecommons.org/licenses/by-nc-nd/4.0/).

1. Introduction

Quantum dots (QDs) have emerged as promising materials for a wide array of optoelectronic applications, encompassing photodetectors, solar cells, lasers, displays, light-emitting diodes, and infrared (IR) image sensors, due to their size-dependent bandgap, solution processability, and ease of synthesis [1–4]. Due to their scientific significance to nanoscience and successful application in the display field, the 2023 Nobel Prize in Chemistry was awarded to three scientists for their groundbreaking work on the discovery and synthesis of QDs. In addition to displays, the QD IR image sensor is another application that is close to widespread commercialization. PbS QDs are typical materials used for QD IR image sensors. Currently, PbS QDs show superior competitiveness compared to non-lead QDs [5]. Because of the solubility and low-temperature processability of PbS QDs, PbS QD thin films can be directly deposited over complementary metal-oxide-semiconductor (CMOS) readout integrated circuits (ROICs), bypassing the flip-chip bonding step that is essential for conventional InGaAs IR image sensors [6]. Thus, QD IR image sensors exhibit good potential for low-cost and large-array (high-resolution) applications and promote the application of IR imaging for machine vision [7], astronomy [8], night monitoring [9], and medical imaging [10].

The synthesis process of PbS QDs plays a crucial role in the development of QD image sensors. First, the quality of PbS QDs

directly affects the performance of image sensors, such as dark current and photoresponse [11]. Second, reducing the cost of PbS QDs is an ongoing pursuit for the large-scale commercialization of QD image sensors. Referring to Jean et al. [12], the preparation cost of PbS QD films (179 USD·m^{-2}) is extremely expensive compared to MAPbI$_3$ (MA: methylammonium, CH$_3$NH$_3^+$) QDs (128 USD·m^{-2}). Various fabrication methods have been developed to reduce the preparation cost of PbS QDs, including hot injection synthesis [13], continuous flow synthesis [14], and heat-up synthesis [15] using typical lead precursors such as PbO [16], Pb(CH$_3$COOH)$_2$ [17], and PbCl$_2$ [18]. The PbCl$_2$-based synthesis not only offers a cost advantage but also improves the PbS QDs devices' performance by providing *in situ* chloride passivation of QD [12,18,19]. Nevertheless, the cost of commercial PbCl$_2$ raw materials still accounts for 20%–45% of the total cost of all raw materials [12]; thus, there is room to further reduce the cost of PbS QDs. This high cost of raw material is ascribed to the preparation of commercial PbCl$_2$, which requires primary lead, which itself normally undergoes a series of energy-intensive and costly processes—a pyrometallurgical process for refining the lead, a ball-milled process to produce lead oxide power and acid leaching. Thus, reducing the cost of PbCl$_2$ and improving its preparation efficiency is crucial for economically synthesizing PbS QDs and thus reducing the cost of their applications.

Synthesizing PbCl$_2$ from secondary lead resources is a cost-effective alternative for preparing the precursor for PbS QDs. For this process, among all the types of secondary lead sources, spent lead paste separated from discarded lead-acid batteries is an ideal and environmentally friendly choice, as it commands 85% of the total lead market [20]. Previously, recycled lead in the form of PbI$_2$ has been used to prepare perovskite materials for solar cells [21–26], demonstrating the success of fabricating devices in an environmentally responsible fashion.

While the recovery of PbCl$_2$ from spent lead paste for PbS QD synthesis is promising, some key challenges remain. One of the major ones is that the composition of spent lead paste is multifaceted, encompassing various constituents such as Pb(II)SO$_4$, which has a high melting point, and lead compounds in three valence states: Pb(IV)O$_2$, Pb(II)O, and metallic Pb^0 [27]. Currently, the main method of recovering PbCl$_2$ from spent lead paste is a high-temperature pyrometallurgical route. However, the pyrometallurgical process releases toxic lead particulates and SO$_2$, which

pose an environmental pollution risk. Additionally, the pyrometallurgical process involves high energy input, with the consumption of coal or natural gas. Therefore, there is an urgent need to develop an environmentally friendly process to recycle high-purity PbCl$_2$ for the synthesis of PbS QDs.

Herein, we report a novel mild hydrometallurgical method for synthesizing high-purity PbCl$_2$ from spent lead paste through a desulfurization and leaching-crystallization route. In contrast to conventional pyrometallurgical or hydrometallurgical methods, this process does not involve SO$_2$ emissions, reduces environmental pollution, and realizes filtrate recirculation. First, high-purity PbCl$_2$ is recovered from spent lead paste using the mild recovery process of desulfurization combined with leaching-crystallization using NaCl–HCl solution. This process has a PbCl$_2$ production ratio of up to 97%. In addition, the preparation cost of recycled PbCl$_2$ (R-PbCl$_2$) using the proposed method is only 27.5% of the cost of commercial PbCl$_2$ (Control). Moreover, employed as a lead precursor to facilitate PbS QDs synthesis using a cation exchange method, R-PbCl$_2$ achieves highly monodispersed and well-passivated PbS QDs. Fabricated IR photodetectors based on these PbS QDs exhibit a dark current density of as low as 23.6 nA·cm^{-2}, a high external quantum efficiency (EQE) of 49.6%, and a specific detectivity of 6.95 × 10^{12} Jones at 1300 nm at −0.01 V bias. Both the quality of the PbS QDs and the performance of the produced photodetectors are comparable to those derived from commercial PbCl$_2$. Furthermore, given the high quality of PbS QDs and the photodetectors derived from R-PbCl$_2$, an IR image sensor is fabricated via a monolithic integration strategy on the CMOS ROIC with a resolution of 640 × 512, and successfully used to discriminate common solvents. This work not only realizes the green recycling of spent lead paste but also provides a low-cost approach for synthesizing PbS QDs and their optoelectronic devices.

2. Results and discussion

2.1. Mild recycling of PbCl$_2$ from spent lead-acid battery paste

2.1.1. Recycling

Fig. 1 illustrates the novel mild hydrometallurgy method for synthesizing high-purity PbCl$_2$ crystals from spent lead-acid battery paste. This efficient synthesis of high-purity PbCl$_2$ comprises
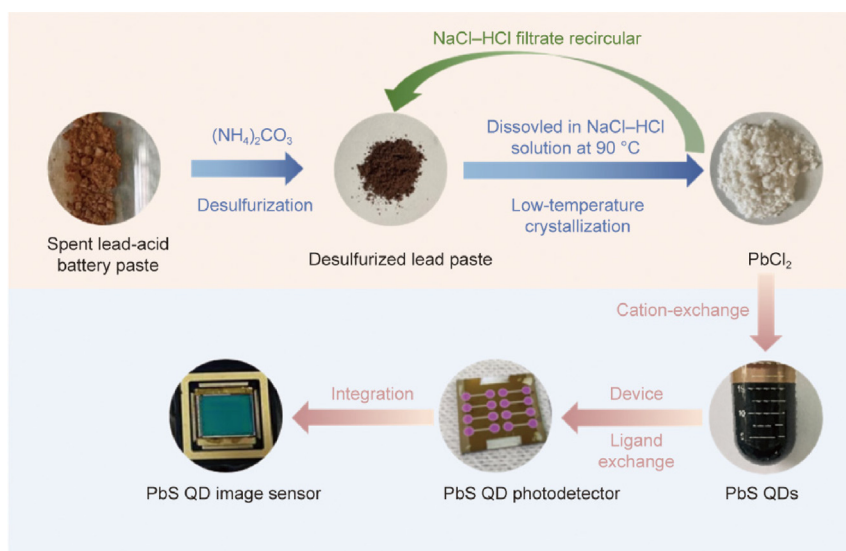

Fig. 1. Recycling process of secondary lead resource from spent lead-acid battery paste for the synthesis of PbS QDs, and their application in IR image sensors

only two steps: desulfurization followed by synchronous reduction and chlorination in the leaching-crystallization step.

The proposed mild hydrometallurgy method does not require a separate reduction step; it combines reduction and halogenation in a single step using NaCl–HCl solution. By comparison, during the pyrometallurgical process, $PbCl_2$ is converted from PbO or refined lead metal [28]; however, PbO and refined lead metal products are normally produced using a smelting process at a high temperature of higher than 1300 °C, which can generate potential lead-containing particles and large amounts of acid gas emissions. The conventional hydrometallurgical process requires separate desulfurization, reduction, and halogenation. The reduction process requires the conversion of Pb(IV) to Pb(II), usually by roasting or acid leaching combined with a reduction agent (i.e., H_2O_2 [29], CH_3OH [22], and metallic Fe [30]).

2.1.2. Desulfurization and chlorination

The process diagram for recovering spent lead paste from spent lead-acid batteries is shown in Fig. 2(a). Analysis of the spent lead paste X-ray diffraction (XRD; Shimadzu-XRD7000, Japan) pattern (Fig. 2(b)) indicates that $PbSO_4$ and PbO_2 were the main phases. The desulfurization process successfully converted 99.85% (Text S1 in Appendix A) of the $PbSO_4$ to $PbCO_3$ at a $(NH_4)_2CO_3/PbSO_4$ molar ratio of 1:3 at 45 °C with a liquid/solid ratio of 8 $mL·g^{-1}$ (Fig. S1 in Appendix A). During this process, sulfate ions were converted to $(NH_4)_2SO_4$ (Eq. (1)), which can be a useful byproduct. The $PbSO_4$ phase in the desulfurized lead paste was sometimes as low as 0.12 wt% (Table S1 in Appendix A). However, the desulfurization process failed to reduce the Pb(IV) of PbO_2 (Fig. 2(b)), and the residual amount of PbO_2 in the desulfurized lead paste was 20.55 wt%. The NaCl–HCl solution was then applied for chlorination. Possible reactions among $PbCO_3$, Pb^0, PbO, and PbO_2 in the desulfurized lead paste with the NaCl–HCl mixed leaching solution are shown in Eqs. (2)–(7). Pb^{2+} can be dissolved into chlorinated compounds in solutions containing excess Cl^-, and the use of NaCl as the chlorine source eliminates the need for excess hydrochloric acid, thereby minimizing the environmental impact. The lead element in the desulfurized lead paste was converted to $PbCl_2$, which can be dissolved in a hot acidic leaching solution in the form of $PbCl_4^{2-}$, $PbCl_3^-$, $PbCl_2$, and $PbCl^+$. After the insoluble impurities in the hot leaching solution were removed by filtration, $PbCl_2$ crystals were obtained by a cooling-crystallization procedure. After the leaching-crystallization step in the synchronous reduction–chlorination process, the production ratio of $PbCl_2$ reached 95.36% when the pH was 1, the liquid/solid ratio (noted as L/S) was 25 $mL·g^{-1}$, and the NaCl concentration was 250 $g·L^{-1}$ (Fig. S2 in Appendix A). The detailed calculation of the production ratio of $PbCl_2$ is presented in Text S2 in Appendix A. The filtrate after the cooling–crystallization procedure was a mixed solvent containing NaCl, HCl, and a small amount of dissolved $PbCl_2$, $NaPbCl_3$, and Na_2PbCl_4, with minor soluble impurities of metal ions (Table S2 in Appendix A). This can be recycled for further leaching reaction batches. The production ratio of $PbCl_2$ in the leaching-crystallization step reached more than 97% (Fig. S3 in Appendix A) because the circulated leaching solution contained residual lead ions that were not crystalized in the previous batch reactions. The main impurities in the spent lead paste—Fe and Ba—mainly remained as $NaFeO_2$ and $BaSO_4$ in the leaching residue after the leaching-crystallization process (Fig. 2(c)). The level as well as the content of impurity in the $R-PbCl_2$ and the commercial $PbCl_2$ were tested
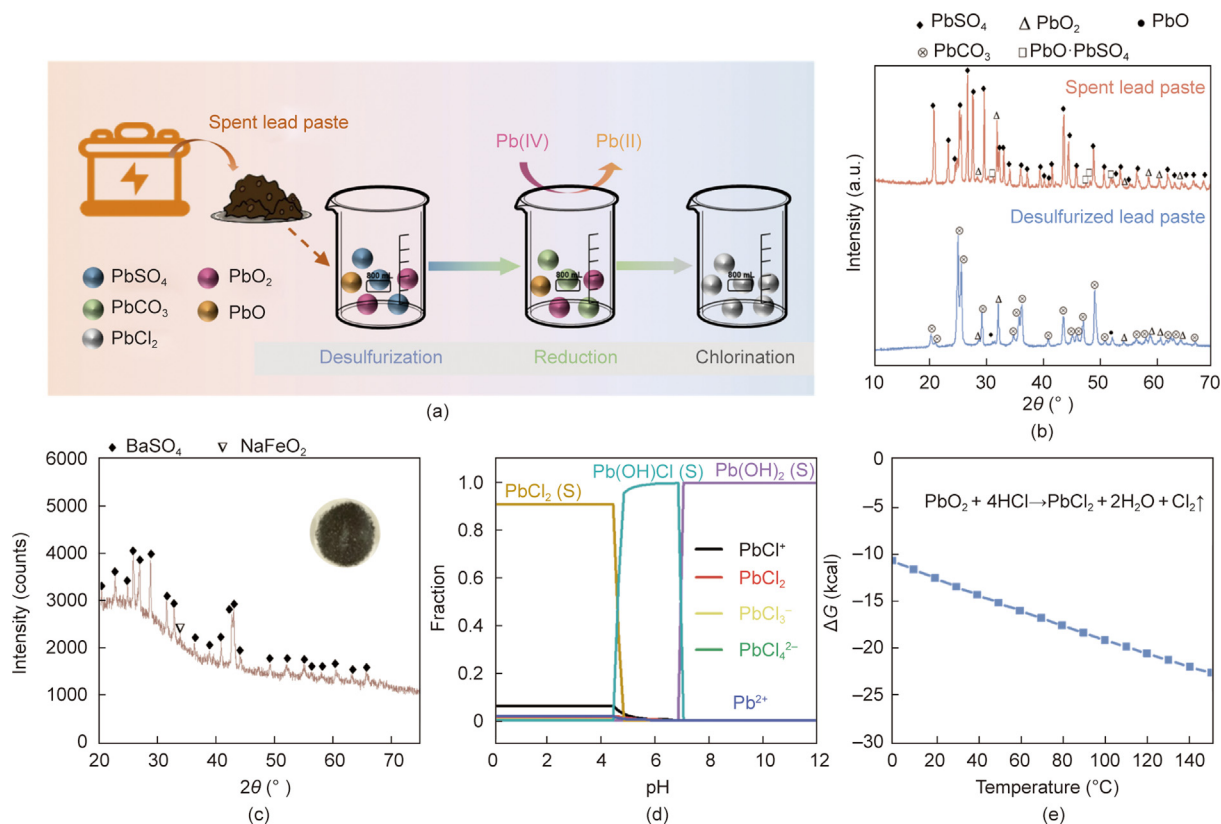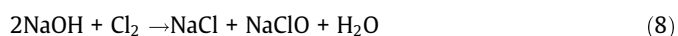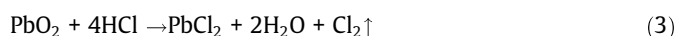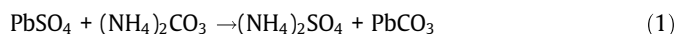

Fig. 2. (a) Schematic of the route of desulfurization and leaching-crystallization from the raw material of spent lead paste; (b) XRD patterns of the spent lead paste and the desulfurized lead paste (2θ: 2 theta-scale); (c) XRD pattern of the leaching residue sample after the leaching-crystallization step in the synchronous reduction–chlorination process; (d) distribution patterns of lead-containing components under different pH conditions (the concentration of $PbCl_2$ and NaCl are 0.1 $mol·L^{-1}$); (e) thermodynamic parameters of reaction between HCl and PbO_2, given by HSC simulation (G: Gibbs free energy).

by using atomic absorption spectroscopy (AAS; Nov AA 400P, Germany; Table S3 in Appendix A) and inductively coupled plasma optical emission spectroscopy (ICP-OES; PerkinElmer Optima 8300, USA; Table S4 in Appendix A). The purity of R-PbCl$_2$ reached 99.99%. The mass balances of the lead and impurities produced during the desulfurization and leaching-crystallization processes are shown in Table S5 in Appendix A. The high-purity PbCl$_2$ crystals were obtained by a simple cooling-crystallization procedure in the leaching solution.

Minteq software (USA) was used to simulate the distribution of lead–containing components in the leaching solution under various pH conditions (Fig. 2(d)). When the pH was less than 4.0, the lead element in the solution mainly existed in the form of a solid PbCl$_2$ phase. When this was combined with the thermodynamic parameters of the reaction between HCl and PbO$_2$ simulated by HSC chemistry software (Finland) (Fig. 2(e)), it was determined that Pb(IV)O$_2$ can be reduced and that chlorination conversion can be improved by adding HCl solution. As shown in Eq. (8), a small amount of released Cl$_2$ gas can be absorbed by the NaOH solution.

$$PbSO_4 + (NH_4)_2CO_3 \rightarrow (NH_4)_2SO_4 + PbCO_3 \tag{1}$$

$$PbCO_3 + 2HCl \rightarrow PbCl_2 + H_2O + CO_2\uparrow \tag{2}$$

$$PbO_2 + 4HCl \rightarrow PbCl_2 + 2H_2O + Cl_2\uparrow \tag{3}$$

$$PbO + 2HCl \rightarrow PbCl_2 + H_2O \tag{4}$$

$$Pb + 2HCl \rightarrow PbCl_2 + H_2\uparrow \tag{5}$$

$$PbCl_2 + 2NaCl \underset{Cooling}{\overset{90\,^\circ C}{\rightleftharpoons}} Na_2PbCl_4 \tag{6}$$

$$PbCl_2 + NaCl \underset{Cooling}{\overset{90\,^\circ C}{\rightleftharpoons}} NaPbCl_3 \tag{7}$$

$$2NaOH + Cl_2 \rightarrow NaCl + NaClO + H_2O \tag{8}$$

The synchronous use of reduction and chlorination processes for the desulfurized lead paste in NaCl–HCl mixing solution removes the more complicated steps of the conventional hydrometallurgical method. Therefore, the as-synthesized PbCl$_2$, with high purity, lays a good foundation for the further production of high-quality PbS QDs and their optoelectronic application.

2.1.3. Characterization of the recycled high-purity PbCl$_2$ product

R-PbCl$_2$ and commercial-PbCl$_2$ control crystals were characterized and tested to determine their crystal structure and purity, respectively. The crystallized morphology of R-PbCl$_2$ was determined by scanning electron microscopy (SEM; JSM-IT200, Japan), shown in Fig. 3(a). The PbCl$_2$ crystal particles were rectangular. In addition, Pb and Cl in the crystallized products were evenly distributed on the surface of the PbCl$_2$ particles (Figs. 3(b) and (c)). The energy dispersive spectrometer (EDS; Oxford 30D, United Kingdom) spectrum of R-PbCl$_2$, presented in Fig. 3(d), reveals that the atomic percentages of Pb and Cl were 34.4% and 65.6%, respectively, which is close to the theoretical ratio (PbCl$_2$) of 1:2. The XRD patterns and X-ray photoelectron spectroscopy (XPS; Thermo Fisher Scientific K-Alpha, USA) spectra of the R-PbCl$_2$ and the control sample are shown in Figs. 3(e)–(g).

Both patterns indicate a single PbCl$_2$ phase, indicating that PbCl$_2$ crystals were successfully synthesized from the spent lead paste. In addition, the results of the peak area fitting of the XPS spectra of Cl and Pb, shown in Table S6 in Appendix A, indicate that their relative atomic percentages were also close to 2:1. As shown

in Fig. 3(g), Pb in both samples was in the form of Pb(II), and the Pb 4f core level did not shift in either sample. High-resolution transmission electron microscopy (HRTEM; FEI Tecnai G2 20, USA) was used to characterize the R-PbCl$_2$ (Figs. 3(h) and (i)). The lattice fringes of R-PbCl$_2$ display interplanar spacings of 0.308 and 0.290 nm in the particle, which match well respectively with those of the (200) and the (201) lattice planes of the face-centered cubic (FCC) PbCl$_2$.

2.2. Synthesis of PbS QDs from the R-PbCl$_2$

The cation exchange method [31,32] was adopted to synthesize the PbS QDs, and the effect of the Pb precursor was investigated. First, PbS QDs with an exciton peak at about 1300 nm were synthesized using the recycled PbCl$_2$ (R-PbS) and the commercial PbCl$_2$ (control sample). The two types of PbS QDs show identical absorption and photoluminescence (PL) spectra, and similar PL quantum yields (PLQYs) by steady-state transient modular fluorescence spectrometer (FLS; HORIBA QuantaMaster 8000, Canada) tests (Fig. 4(a) and Fig. S4 in Appendix A), and the XRD characterization results are similar (Fig. S5 in Appendix A). In addition, the control PbS QDs and the R-PbS QDs, with exciton peaks of 940 and 1700 nm, respectively, were synthesized for comparison. As shown in Fig. 4(b), the control PbS QDs and the R-PbS QDs had the same quality for different exciton peaks (sizes) in terms of the absorption spectrum. Furthermore, using R-PbCl$_2$, a series of R-PbS QDs were synthesized, that had a wide exciton peak range covering a large range of 940–1867 nm (Fig. 4(c)). All spectra show sharp exciton peaks similar to previously published results [33], indicating the highly uniform sizes of these R-PbS QDs. The TEM images of the R-PbS QDs with exciton peaks at 1700 and 1236 nm are shown in Figs. 4(d) and (e), respectively. The size distribution data of PbS QDs with exciton peaks located at 1700 and 1236 nm were obtained by counting 220 and 250 PbS QDs, respectively. For the 1236 nm-PbS QDs, the size and size distribution were 4.43 nm and 7.2%, respectively, while the values for the 1700 nm-PbS QDs were 6.48 nm and 6.8%, respectively. The QDs had a uniformly spherical shape and high monodispersity, as demonstrated by their ordered self-assembly. Therefore, these comparative experiments demonstrated the very similar properties of the R-PbS QDs and the control PbS QDs, confirming the feasibility of producing high–performance PbS QDs directly derived from the secondary lead resource by using the proposed novel recovery processes.

2.3. Device performance

PbS QD detectors were prepared according to the structure of ITO/SnO$_2$/C$_{60}$/PbS/PbS–EDT/NiO$_x$ (ITO: indium–tin oxides, EDT: 1,2-ethanedithiol) (Fig. 5(a)), and the corresponding cross-section SEM image is presented in Fig. 5(b). Various measurements were conducted to compare the basic characteristics of devices made from the R-PbCl$_2$ and the control sample. Fig. 5(c) shows the current density–voltage (J–V) curves of the devices under 1300 nm light-emitting diode (LED) illumination. The detectors show rectification ratios of over three orders of magnitude and excellent optical response. Fig. 5(d) shows the statistical results of the dark current density (J_{dark}) and EQE of 23 detectors made from the R-PbCl$_2$ and the control sample. The R-PbCl$_2$ devices show performances comparable to those of the control devices. Both the J_{dark} and EQE show good repeatability. The devices made from the R-PbCl$_2$ exhibit an average J_{dark} of 23.6 nA·cm^{-2} at −0.01 V bias and an average EQE of 49.6%, which are comparable to current world-leading devices with similar response peaks of about 1300 nm (Fig. 5(e) and Table 1 [6,34–36]). Based on the measured noise power density (Fig. S6 in Appendix A), the specific detectivities (D^*) were calculated to be 6.95 $\times$ 10^{12} and
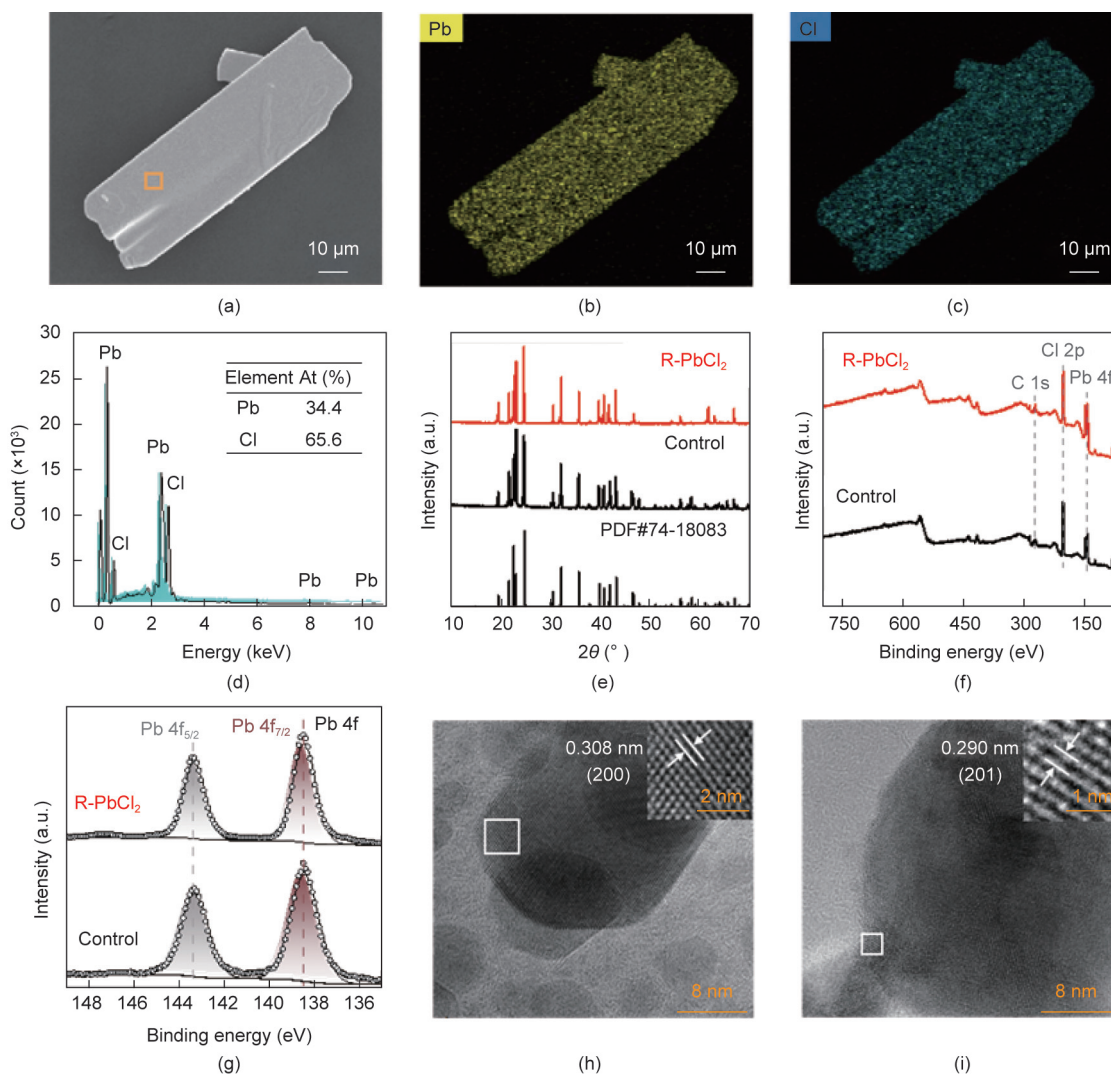
Fig. 3. Characterization of the recycled products from spent lead-acid battery paste (R-PbCl$_2$) and high-purity commercial PbCl$_2$ (Control). (a) SEM image of R-PbCl$_2$, (b) Pb element mapping in R-PbCl$_2$; (c) Cl element mapping in R-PbCl$_2$; (d) EDS spectrum of the R-PbCl$_2$ sample (At%: atomic percent); (e) XRD patterns of the R-PbCl$_2$ and control samples (PDF: powder diffraction file); (f) XPS spectra of the PbCl$_2$ samples; (g) core XPS spectra of PbCl$_2$ in Pb 4f binding energy ranges, and (h, i) high-resolution transmission electron microscopy (HRTEM) image of R-PbCl$_2$ sample.

4.76×10^{12} Jones for the R-PbCl$_2$ and control samples, respectively, confirming the similar performance of the two types of devices.

Based on the high-performance PbS QD photodetectors made from the R-PbCl$_2$, a short-wave infrared (SWIR) image sensor was fabricated by depositing the PbS QD photodetector onto a CMOS ROIC with a pixel array of 640×512 (Fig. 5(f)). The prepared PbS quantum dots SWIR image sensor is a complex system, and the detail of synthesis can be obtained from our previous studies [37,38]. To demonstrate the material identification capability of the SWIR image sensor, an image of water and tetrachloroethylene (TCE) captured by the imager under irradiation from a 1300 nm planar light source is shown in Fig. 5(g). Compared to the visible light image, the SWIR image shows that the water is darker than the TCE because water has a stronger absorbance at 1300 nm than does TCE. Material identification capabilities and IR imaging are appealing functions of SWIR imagers, which are important supplements to visible light imagers. PbS QD image sensors are promising alternative chips for a wide range of applications due to their low cost via monolithic integration. These results show that it is possible to fabricate high-performance PbS QD image sensors using recycled Pb precursors from spent lead paste, providing a low-cost and environmentally friendly strategy for QD imagers.

In addition to photodetectors, another type of optoelectronic device, solar cells, was also fabricated using R-PbCl$_2$ (Fig. S7 in Appendix A). Through the solar simulation system of xenon lamp source (NEWPORT Model 9119, USA) test, the average power conversion efficiency of the solar cells made from the R-PbCl$_2$ was 9.31%, which is comparable to that of devices made from the commercial PbCl$_2$ (9.58%), further confirming the excellent optoelectronic properties of PbS QDs synthesized from R-PbCl$_2$ (Table S8 in Appendix A).

2.4. Technoeconomic analysis

Fig. 6(a) summarizes the current pyrometallurgical (Pyro-) and conventional hydrometallurgical (Conv. hydro-) recycling processes for preparing PbCl$_2$ from spent lead-acid batteries, and compares them with our novel mild hydrometallurgical (Mild hydro-) method introduced in this work. Assuming one metric tonne of spent lead-acid batteries, we analyzed and compared the economic value and environmental impact of these three technologies based on the proportion of each component and the recovery process. A detailed analysis of the material flow was conducted (Fig. S8 in Appendix A), and specific calculations for the technoeconomic
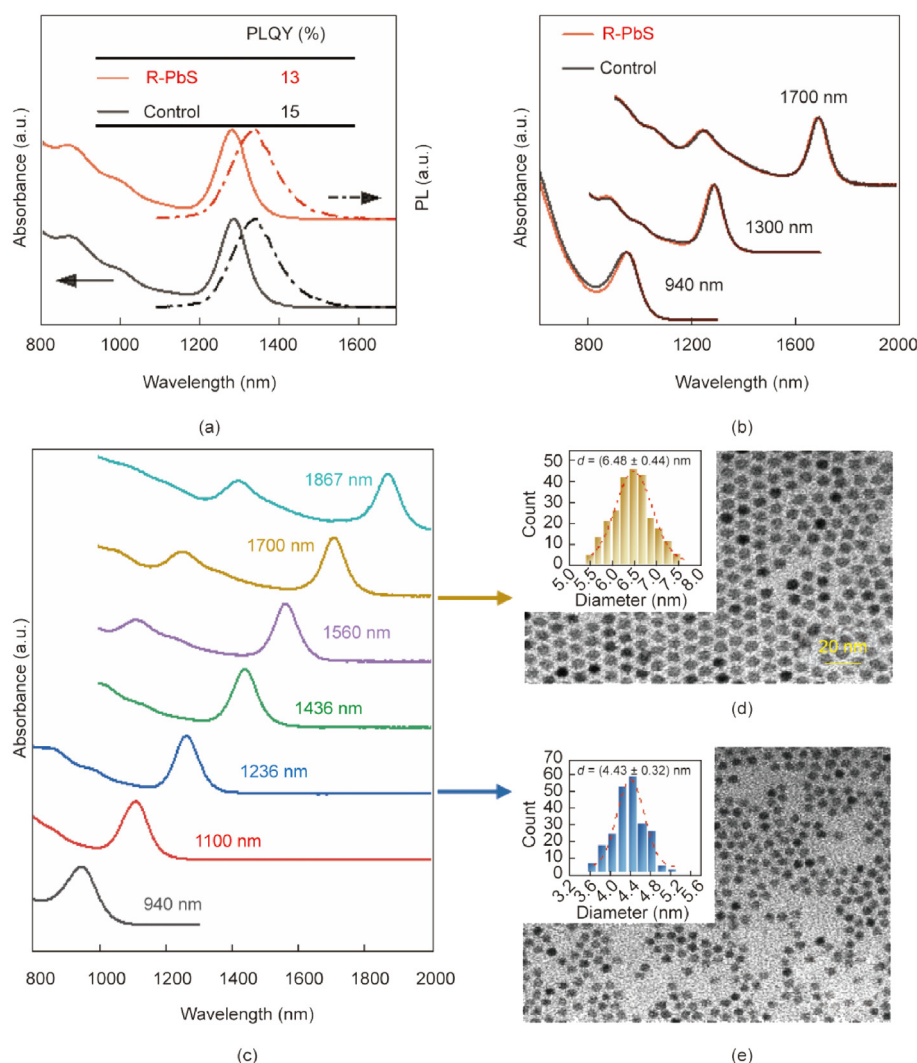
Fig. 4. (a) Absorption spectra and PL (dashed line) spectra of PbS QDs (with exciton peaks of ~1300 nm) synthesized from the R-PbCl$_2$ and the control sample; (b) close comparison of the absorption peaks of three typical PbS QDs synthesized from the R-PbCl$_2$ and the control sample; (c) a series of absorption spectra of PbS QDs synthesized by the R-PbCl$_2$; (d, e) TEM images and particle size distributions (*d*) of PbS QDs with exciton peaks of (d) 1700 and (e) 1236 nm.

analysis are provided in the Text S3 in Appendix A. The recycling processes (Tables S9–S11 in Appendix A) are presented according to the process system boundary shown in Fig. S8, and the environmental impacts of the three recycling processes were evaluated using the life-cycle assessment (LCA) method. The calculated results of five characteristic indexes—global warming potential (GWP), primary energy demand (PED), acidification potential (AP), human toxicity potential (HTP), and terrestrial ecotoxicity potential (TETP)—are shown in Table S12 in Appendix A. As shown in Fig. 6(b), the performance of the novel hydrometallurgical method is generally superior to that of the pyrometallurgical process across these five indexes. In addition, mild hydrometallurgy has a great advantage in the green use of chemical reagents (Fig. 6(c)). Compared with the two hydrometallurgical processes, mild hydrometallurgy performs better than conventional hydrometallurgy for GWP, PED, HTP, and TETP. The mild hydrometallurgy itself is slightly flawed in terms of acidification, eutrophication, and ozone depletion, due to the use of (NH$_4$)$_2$CO$_3$ and HCl, which leads to characteristic pollutants such as NH$_3$, CO$_2$, and Cl$_2$ in the process. Combined with the proportions of the various costs of these recovery processes (Fig. 6(d) and Fig. S8 in Appendix A), mild hydrometallurgy has the obvious

advantages of reduced reagent cost and environmental impact compared to conventional hydrometallurgy. In accordance with commonly reported pyrometallurgical and conventional hydrometallurgical processes, approximately 590 kg (Fig. S8(a)) and 561 kg of PbCl$_2$ (Fig. S8(b)) were obtained from spent lead paste, resulting in profit generation amounts of 8287 and 3285 USD, respectively (Fig. 6(e)). In contrast, recycling one metric tonne of spent lead-acid batteries using the novel hydrometallurgy method yielded 572 kg PbCl$_2$ (Fig. S8(c)), equivalent to an profit of 11 163 USD (Fig. 6(e)). According to the calculation, the raw material price of PbCl$_2$ accounts for 32.40% of the total cost of synthesized PbS QDs (Table S15 in Appendix A and Fig. 6(f)). The method proposed in this study can reduce the raw material cost of PbCl$_2$ by 72.5%. The synthesis cost of PbS QDs can be reduced by 23.2% by using the PbCl$_2$ recycled in this study, and each synthesized metric tonne of PbS QDs can generate about 17 000 USD more profit than using commercial PbCl$_2$ (Fig. 6(g)).

3. Conclusions

A novel environmentally friendly hydrometallurgical method for recycling spent lead-acid battery paste into high-purity PbCl$_2$
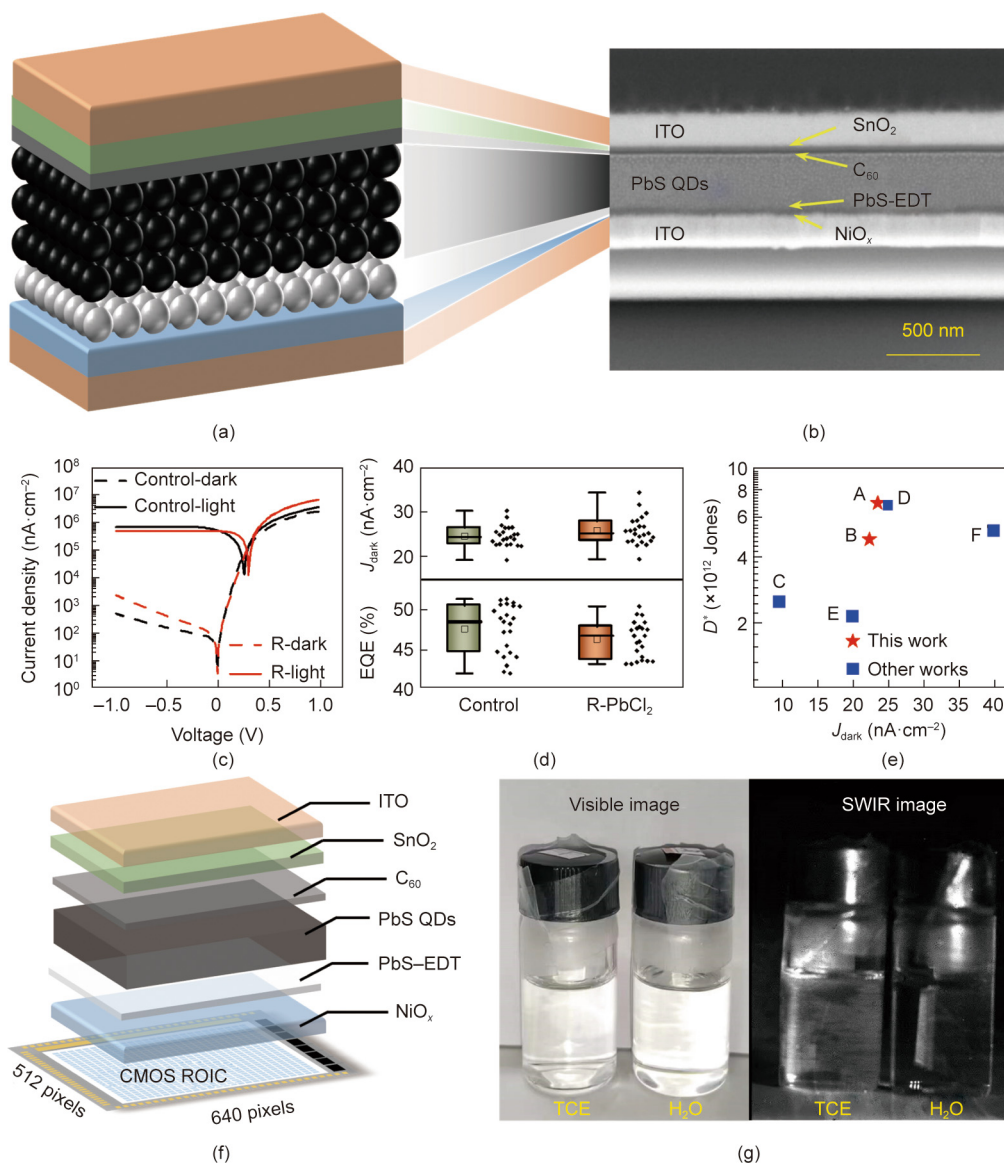
Fig. 5. PbS QD (with an exciton peak of ∼1300 nm) photodetectors and image sensors. (a) Structure diagram, (b) cross-section SEM image, (c) steady-state response of photodetectors based on PbS QDs synthesized from control and recycled PbCl$_2$, respectively, (d) J_{dark} and EQE of PbS QD photodetectors, (e) specific detectivity (D^*) and J_{dark} of PbS QD photodetectors reported in the literature. The corresponding materials and documents are shown in Table 1 [6,34–36]. (f) The structure of the PbS QD short-wave infrared (SWIR) image sensor, (g) photographs captured using the PbS QD SWIR image sensor and visible image sensor.

that achieved a 97% PbCl$_2$ production ratio was developed. The quality of the R-PbCl$_2$ is comparable to that of commercially sourced PbCl$_2$. The R-PbCl$_2$ was successfully employed to synthesize PbS QDs, and their performance was comparable to those synthesized from commercial PbCl$_2$. Furthermore, PbS QD photodetectors derived from R-PbCl$_2$ showed similar performance levels compared to devices derived from commercial lead precursors in terms of J_{dark}, EQE, and specific detectivity. Based on these high-performance photodetectors, a CMOS monolithically integrated PbS QD image sensor was fabricated from R-PbCl$_2$ for the first time, and was successfully applied to discriminate common solvents. These results demonstrate that R-PbCl$_2$ from spent lead-acid battery paste provides a low-cost lead precursor for the synthesis of PbS QDs and their application in optoelectronic devices. The calculated cost of synthesized PbCl$_2$ using this recycling method was 27.5% of the cost of commercial PbCl$_2$. This study provides a novel hydrometallurgical recovery route to synthesize PbCl$_2$ derived from spent lead paste, and an economically valuable route for producing upstream materials for PbS QD optoelectronic devices.

CRediT authorship contribution statement

Yuxin Tong: Writing – original draft, Visualization, Methodology, Data curation. **Dijie Zhang:** Writing – review & editing, Visualization, Methodology, Data curation. **Zhaoyang Li:** Methodology, Formal analysis, Data curation. **Guang Hu:** Writing – review & editing, Formal analysis. **Qingfang Zou:** Writing – review & editing. **Luna Xiao:** Formal analysis, Data curation. **Weidong Wu:** Formal analysis, Data curation. **Liang Huang:** Writing – review & editing, Methodology, Formal analysis. **Sha Liang:** Writing – review & editing, Methodology, Formal analysis. **Huabo Duan:** Writing – review & editing, Methodology, Formal analysis. **Jingping Hu:** Writing – review & editing, Formal analysis. **Huijie Hou:** Writing – review & editing, Formal analysis. **Jianbing Zhang:** Writing – review &

Table 1

Comparison of device performances of the reported PbS QD photodetectors with similar response peaks of about 1300 nm

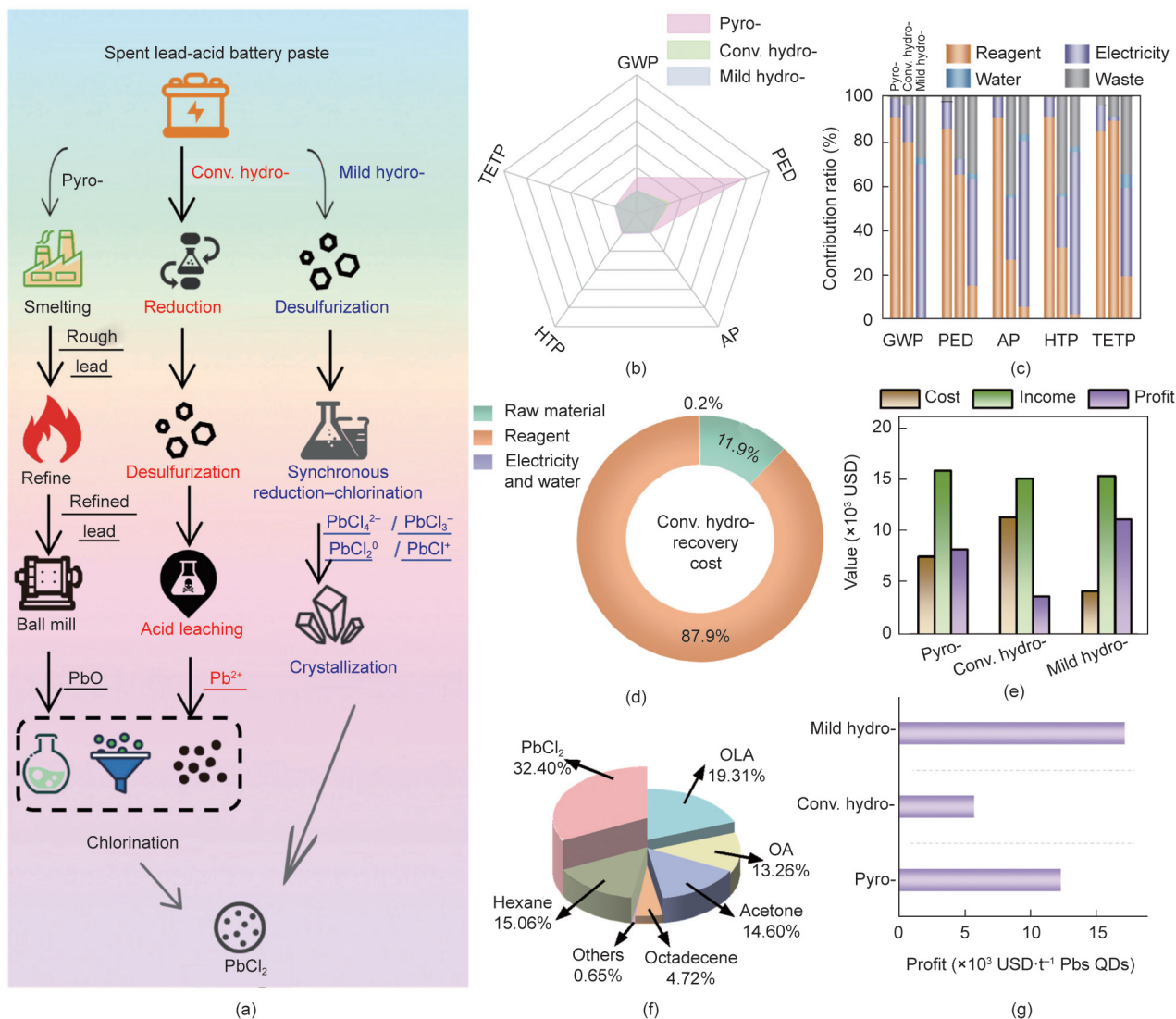| Item	Lead precursor	Source	Structure	EQE (%)	J_{dark} @−0.01V (nA·cm^{-2})	D^* (Jones)
A	R-PbCl$_2$	This work	ITO/SnO$_2$/C$_{60}$/PbS/PbS–EDT/NiO$_x$	49.6	23.6	6.95×10^{12}
B	Control commercial PbCl$_2$ sample	This work	ITO/SnO$_2$/C$_{60}$/PbS/PbS–EDT/NiO$_x$	50.2	22.4	4.76×10^{12}
C	Control commercial PbCl$_2$ sample	[6]	ITO/ZnO/CQDs-I/CQDs-EDT/Au	50.8	9.6	2.5×10^{12}
D	Control commercial PbCl$_2$ sample	[34]	ITO/ZnO/PbS-I&Br/PbS-EDT/Au	~50	~25	6.8×10^{12}
E	Control commercial PbCl$_2$ sample	[35]	ITO/Sputtered-ZnO/PbS/PbS-EDT/Au	50.28	~20	2.15×10^{12}
F	Control commercial PbCl$_2$ sample	[36]	ITO/ZnO/PbS-I/PbS-EDT/Au	22.9	~40	5.22×10^{12}

Fig. 6. (a) Comparison diagram of extraction process of lead chloride from spent lead-acid battery paste by pyrometallurgical process, conventional (Conv.) hydrometallurgical process, and proposed mild process; (b) environmental impacts of the three recycling processes; (c) environmental impact contribution of each part of the three recycling processes; (d) pie chart showing the cost proportions based on the conventional hydro-recovery process; (e) economic analysis of the three recycling processes; (f) cost and proportion of raw materials needed to synthesize PbS QDs; (g) profit calculations for the synthesis of PbS QDs by the three recycling processes. OLA: oleylamine, OA: oleic acid.

editing, Supervision, Conceptualization. **Jiakuan Yang:** Writing – review & editing, Supervision, Funding acquisition, Conceptualization.

Declaration of competing interest

The authors declare that they have no known competing financial interests or personal relationships that could have appeared to influence the work reported in this paper.

University of Science and Technology (HUST) and the School of Environmental Science and Engineering Environment of HUST for materials analysis.

Appendix A. Supplementary data

Supplementary data to this article can be found online at https://doi.org/10.1016/j.eng.2024.11.003.

References

[1] Sun B, Najarian AM, Sagar LK, Biondi M, Choi MJ, Li XY, et al. Fast near-infrared photodetection using III–V colloidal quantum dots. Adv Mater 2022;34 (33):2203039.

[2] Choi YK, Kim TH, Jung BK, Park T, Lee YM, Oh S, et al. High-performance self-powered quantum dot infrared photodetector with azide ion solution treated electron transport layer. Small 2024;20(18):2308375.

[3] Li JL, Qiu JW, Xie B, Li WH, Wang K, Suk CH, et al. Light-emitting MOS junction for ultrahigh-resolution quantum dot displays. Nano Energy 2024;120:109105.

[4] Vafaie M, Fan JZ, Morteza Najarian A, Ouellette O, Sagar LK, Bertens K, et al. Colloidal quantum dot photodetectors with 10-ns response time and 80% quantum efficiency at 1,550 nm. Matter 2021;4(3):1042–53.

[5] Wang Y, Peng L, Schreier J, Bi Y, Black A, Malla A, et al. Silver telluride colloidal quantum dot infrared photodetectors and image sensors. Nat Photonics 2024;18(3):236–42.

[6] Jung BK, Yoo H, Seo B, Choi HJ, Choi YK, Kim TH, et al. High-affinity ligand-enhanced passivation of group III–V colloidal quantum dots for sensitive near-infrared photodetection. ACS Energy Lett 2024;9(2):504–12.

[7] Tang Y, Chen M, Wang C, Luo L, Li J, Lian G, et al. Recognition and localization methods for vision-based fruit picking robots: a review. Front Plant Sci 2020;11:510.

[8] Schödel R, Ott T, Genzel R, Hofmann R, Lehnert M, Eckart A, et al. A star in a 15.2-year orbit around the supermassive black hole at the centre of the Milky Way. Nature 2002;419(6908):694–6.

[9] Lu HP, Carroll GM, Neale NR, Beard MC. Infrared quantum dots: progress, challenges, and opportunities. ACS Nano 2019;13:939–53.

[10] Lim YT, Kim S, Nakayama A, Stott NE, Bawendi MG, Frangioni JV. Selection of quantum dot wavelengths for biomedical assays and imaging. Mol Imaging 2003;2(1):50–64.

[11] Jung BK, Woo HK, Shin C, Park T, Li N, Lee KJ, et al. Suppressing the dark current in quantum dot infrared photodetectors by controlling carrier statistics. Adv Opt Mater 2022;10(2):2101611.

[12] Jean J, Xiao J, Nick R, Moody N, Nasilowski M, Bawendi M, et al. Synthesis cost dictates the commercial viability of lead sulfide and perovskite quantum dot photovoltaics. Energy Environ Sci 2018;11(9):2295–305.

[13] Moreels I, Justo Y, Geyter BD, Haustraete K, Martins JC, Hens Z. Size-tunable, bright, and stable PbS quantum dots: a surface chemistry study. ACS Nano 2011;5(3):2004–12.

[14] Stavrinadis A, Rath AK, de Arquer FPG, Diedenhofen SL, Magen C, Martinez L, et al. Heterovalent cation substitutional doping for quantum dot homojunction solar cells. Nat Commun 2013;4(1):2981.

[15] Zhang JB, Gao JB, Miller EM, Luther JM, Beard MC. Diffusion-controlled synthesis of PbS and PbSe quantum dots with in situ halide passivation for quantum dot solar cells. ACS Nano 2014;8(1):614–22.

[16] Yarema M, Yarema O, Lin WMM, Volk S, Yazdani N, Bozyigit D, et al. Upscaling colloidal nanocrystal hot-injection syntheses via reactor underpressure. Chem Mater 2017;29(2):796–803.

[17] Chang LY, Lunt RR, Brown PR, Bulović V, Bawendi MG. Low-temperature solution-processed solar cells based on PbS colloidal quantum dot/CdS heterojunctions. Nano Lett 2013;13(3):994–9.

[18] Huang Z, Zhai GM, Zhang ZM, Zhang CW, Xia Y, Lian LY, et al. Low cost and large scale synthesis of PbS quantum dots with hybrid surface passivation. CrystEngComm 2017;19(6):946–51.

[19] Wang YJ, Liu ZK, Huo NJ, Li F, Gu MF, Ling XF, et al. Room-temperature direct synthesis of semi-conductive PbS nanocrystal inks for optoelectronic applications. Nat Commun 2019;10(1):5136.

[20] Zhang W, Yang JK, Wu X, Hu YC, Yu W, Wang J, et al. A critical review on secondary lead recycling technology and its prospect. Renew Sustain Energy Rev 2016;61:108–22.

[21] Chen PY, Qi JF, Klug MT, Dang XN, Hammond PT, Belcher AM. Environmentally responsible fabrication of efficient perovskite solar cells from recycled car batteries. Energy Environ Sci 2014;7(11):3659–65.

[22] Li C, Zhu Z, Wang Y, Guo Q, Wang C, Zhong P, et al. Lead acetate produced from lead-acid battery for efficient perovskite solar cells. Nano Energy 2020;69:104380.

[23] Li J, Duan CH, Yuan LG, Liu ZD, Zhu HP, Ren JW, et al. Recycling spent lead-acid batteries into lead halide for resource purification and multifunctional perovskite diodes. Environ Sci Technol 2021;55(12):8309–17.

[24] Wang JX, Yang JK, Hou HJ, Li W, Hu JP, Li MY, et al. A green strategy to synthesize two-dimensional lead halide perovskite via direct recovery of spent lead-acid battery. Resour Conserv Recycling 2021;169:105463.

[25] Xie LS, Zeng Q, Li QY, Wang SR, Li LH, Li ZY, et al. A green lead recycling strategy from used lead acid batteries for efficient inverted perovskite solar cells. J Phys Chem Lett 2021;12(39):9595–601.

[26] Hu L, Li QY, Yao YC, Zeng Q, Zhou ZZ, Cazorla C, et al. Perovskite quantum dot solar cells fabricated from recycled lead-acid battery waste. ACS Mater Lett 2022;4:120–7.

[27] Ma C, Shu YH, Chen HY. Preparation of high-purity lead oxide from spent lead paste by low temperature burning and hydrometallurgical processing with ammonium acetate solution. RSC Advances 2016;6(25):21148–55.

[28] Ballantyne AD, Hallett JP, Riley DJ, Shah N, Payne DJ. Lead acid battery recycling for the twenty-first century. R Soc Open Sci 2018;5(5):171368.

[29] Li M, Yang J, Liang S, Wang J, Zhang P, Yu W, et al. A closed-loop ammonium salt system for recovery of high-purity lead tetroxide product from spent lead-acid battery paste. J Clean Prod 2020;250:119488.

[30] Yu WH, Yang JK, Liang S, Zhang PY, Li MY, Wang JX, et al. Role of iron impurity in hydrometallurgical recovery process of spent lead-acid battery: phase transformation of positive material made from recovered leady oxide. J Electrochem Soc 2019;166(10):A1715–24.

[31] Zhang JB, Chernomordik BD, Crisp RW, Kroupa DM, Luther JM, Miller EM, et al. Preparation of Cd/Pb chalcogenide heterostructured janus particles via controllable cation exchange. ACS Nano 2015;9(7):7151–63.

[32] Zhang CW, Xia Y, Zhang ZM, Huang Z, Lian LY, Miao XS, et al. Combination of cation exchange and quantized ostwald ripening for controlling size distribution of lead chalcogenide quantum dots. Chem Mater 2017;29 (8):3615–22.

[33] Xia Y, Liu SS, Wang K, Yang XK, Lian LY, Zhang ZM, et al. Cation-exchange synthesis of highly monodisperse PbS quantum dots from ZnS nanorods for efficient infrared solar cells. Adv Funct Mater 2020;30(4):1907379.

[34] Wang Y, Hu HC, Yuan M, Xia H, Zhang XC, Liu J, et al. Colloidal PbS quantum dot photodiode imager with suppressed dark current. ACS Appl Mater Interfaces 2023;15(50):58573–82.

[35] Lu SC, Liu PL, Yang Li, Liu SJ, Yang Y, Chen L, et al. High-performance colloidal quantum dot photodiodes via suppressing interface defects. ACS Appl Mater Interfaces 2023;15(9):12061–9.

[36] Yang JR, Lu SC, Xia B, Liu PL, Yang Y, Xiao ZW, et al. Excess PbBr$_2$ passivation of large PbS colloidal quantum dots to reduce dark-current density for near-infrared detection. Phys Rev Appl 2023;19(1):014021.

[37] Liu Y, Liu J, Deng C, Wang B, Xia B, Liang X, et al. Planar cation passivation on colloidal quantum dots enables high-performance 0.35–1.8 μm broadband TFT imager. Adv Mater 2024;36(21):2313811.

[38] Liu P, Lu S, Liu J, Xia B, Yang G, Ke M, et al. Double-ended passivator enables dark-current-suppressed colloidal quantum dot photodiodes for CMOS-integrated infrared imagers. InfoMat 2024;6(1):e12497.